

One-Vote Veto: A Self-Training Strategy for Low-Shot Learning of a Task-Invariant Embedding to Diagnose Glaucoma

Rui Fan, Christopher Bowd, Nicole Brye, Mark Christopher,
Robert N. Weinreb, David Kriegman, Linda Zangwill
UC San Diego

{rfan, cbowd, nbrye, mac157, rweinreb, kriegman, lzungwill}@ucsd.edu

Abstract

Convolutional neural networks (CNNs) are a promising technique for automated glaucoma diagnosis from images of the fundus, and these images are routinely acquired as part of an ophthalmic exam. Nevertheless, CNNs typically require a large amount of well-labeled data for training, which may not be available in many biomedical image classification applications, especially when diseases are rare and where labeling by experts is costly.

This paper makes two contributions to address this issue: (1) It introduces a new network architecture and training method for low-shot learning when labeled data are limited and imbalanced, and (2) it introduces a new semi-supervised learning strategy that uses additional unlabeled training data to achieve great accuracy. Our multi-task twin neural network (MTTNN) can use any backbone CNN, and we demonstrate with ResNet-50 and MobileNet-v2 that its accuracy with limited training data approaches the accuracy of a finetuned backbone trained with a dataset that is 50 times larger. We also introduce One-Vote Veto (OVV) self-training, a semi-supervised learning strategy, that is designed specifically for MTTNNs. By taking both self-predictions and contrastive-predictions of the unlabeled training data into account, OVV self-training provides additional pseudo labels for finetuning a pretrained MTTNN. Using a large dataset with more than 50,000 fundus images acquired over 25 years, extensive experimental results demonstrate the effectiveness of low-shot learning with MTTNN and semi-supervised learning with OVV. Three additional, smaller clinical datasets of fundus images acquired under different conditions (cameras, instruments, locations, populations), are used to demonstrate generalizability of the methods. Source code and pretrained models will be publicly available upon publication.

1. Introduction

Glaucoma is a blinding but treatable disease in which damage to the optic nerve can result in progressive and ir-

reversible vision loss [56]. In 2013, glaucoma affected an estimated 64.3 million individuals worldwide [51]. Because of the rapid global increase in aging populations, 111.8 million cases are expected by 2040 [51]. Improvement in the management of glaucoma would have a major human and socio-economic impact. Early identification would significantly reduce the economic burden of this disease in its late stages [52]. In addition, studies have shown that visual impairment in glaucoma patients are associated with overall decreases in self-reported vision-related physical activity and mental health [18, 38] as well as an increased risk of involvement in motor vehicle accidents [26, 35].

With recent advances in machine learning, convolutional neural networks (CNNs), trained by supervised learning, have shown their potential to become an effective tool to diagnose glaucoma from fundus images, photographs of the back of eyes [28]. To achieve this, very large amounts of empirical data are required for supervised training (see Fig. 1). For this work, we use 66715 fundus photographs from the Ocular Hypertension Treatment Study (OHTS) [15, 21, 14], a 22-site multi-center, longitudinal (1994-2019) randomized clinical trial of 1636 subjects. The primary goal of the OHTS [15] was to determine if topical ocular hypotensive medications could delay or prevent the onset of glaucoma in eyes with high intraocular pressure. Conversion to glaucoma was decided by a masked endpoint committee of three glaucoma specialists using fundus photographs and visual fields. Owing to its well-characterized ground truth labels, the OHTS dataset [15, 21] provides us a basis to explore an effective way of training CNNs to diagnose glaucoma with low-shot learning (LSL) and/or semi-supervised learning (SSL), when only a small quantity of labeled data are available. This is a promising research area that requires more attention, because of its potential to be applied to other biomedical image analysis tasks, where supervised learning often suffers from small sample size issues. However, as shown in Fig. 1, (inductive) SSL typically requires a reliable pretrained CNN (using a small sample) as prior knowledge. Providing such a CNN is often

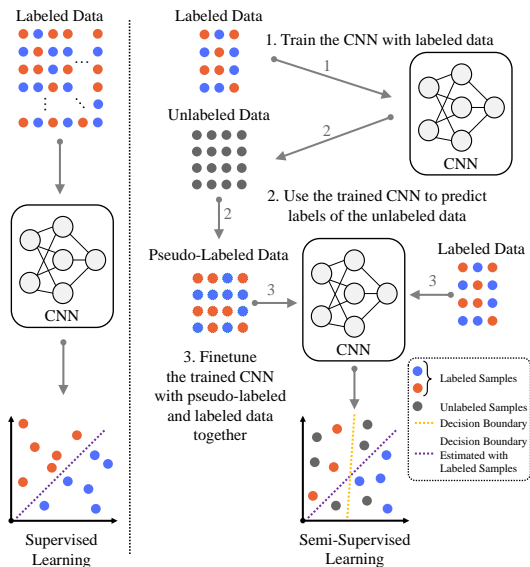


Figure 1: Supervised learning vs. semi-supervised learning.

challenging due to the overfitting problem. Moreover, there is also a strong motivation to design a feasible SSL strategy which is capable of determining confident predictions and generating pseudo labels for unlabeled data. Therefore, this paper aims at answering the following questions:

1. Can a CNN be developed to accurately diagnose glaucoma compared to the expert graders of the OHTS [15, 21, 14]? Will the model be generalizable to other datasets?
2. Is it necessary to train CNNs with thousands of labeled fundus images to diagnose glaucoma? Can we use only one image from each patient (around 1.1K fundus images in total in the training set)?
3. Can performance be improved further when the CNN trained using a small sample is finetuned by SSL with more unlabeled training data?

To answer these questions, we first use ResNet-50 [16], the most commonly utilized CNN for glaucoma diagnosis [29, 39, 36, 8, 9], as the backbone CNN to explore the feasibility of training a multi-task twin neural network (MTTNN) to diagnose glaucoma with only 1147 fundus images (one image from each patient). Additionally, developing low-cost and real-time embedded glaucoma diagnosis systems for mobile devices is also an emerging area [19, 33, 50]. In this regard, we also use MobileNet-v2 [42] as an alternative backbone in a MTTNN. Furthermore, we propose an effective SSL strategy, referred to as One-Vote Veto (OVV) self-training, to generate confident pseudo labels of the unlabeled training data, which are then added into the labeled training data to finetune the CNNs for better performance and generalization ability. Extensive experimental results demonstrate that by using such a MTTNN, the overfitting problem can be reduced, and the achieved

area under the receiver operating characteristic curve (AUROC or simply AUC) is only slightly lower than that of the backbone CNN trained with 53K fundus images under full supervision. Furthermore, the MTTNNs finetuned with OVV self-training perform similarly to the corresponding backbone CNNs trained via supervised learning on the OHTS [14] test set, and with higher AUC on three additional independent clinical datasets.

2. Related Work

2.1. Image Classification

AlexNet [25] is one of the modern CNNs that pushed image classification accuracy significantly. VGG architectures [43] improved over AlexNet [25] by increasing the network depth, which enabled them to learn more complicated image features. However, VGG architectures consist of hundreds of millions of parameters, making them very memory-consuming. GoogLeNet [46] (also known as Inception-v1) and Inception-v3 [47] go deeper in parallel paths with different receptive field sizes, so that the Inception module can act as a multi-level image feature extractor. Compared to VGG [43] architectures, GoogLeNet [46] and Inception-v3 [47] have lower computational complexity.

However, with the increase of network depth, accuracy gets saturated and then degrades rapidly [16], due to vanishing gradients. To tackle this problem, [16] introduces residual neural network (ResNet). It is comprised of a stack of building blocks, each of which utilizes identity mapping (skip connection) to add the output from the previous layer to the layer ahead. This helps gradients propagate. Due to its robustness, ResNet-50 [16] has been extensively used for biomedical image analysis, and it is a common choice [29, 39, 36, 8, 9] for fundus image classification.

In recent years, researchers have turned their focus to light-weight CNNs, which can be embedded in mobile devices to perform real-time image classification. MobileNet-v2 [42], ShuffleNet-v2 [31], and MNASNet [49] are three of the most popular CNNs of this kind. MobileNet-v2 [42] mainly introduces the inverted residual and linear bottleneck layer, which allows high accuracy and efficiency in mobile vision applications. We chose to use ResNet-50 [16] and MobileNet-v2 [42] as the backbone CNNs in our experiments as they are two representative CNNs used in medical image analysis and disease detection problems.

2.2. Low-Shot Learning

Machine/deep learning has achieved compelling performance in data-intensive applications, but it is often difficult when the training size is small [55]. LSL came into existence to this end. Existing LSL algorithms can be categorized into four classes: 1) multi-task learning, 2) embedding learning, 3) learning with external memory, and 4) gen-

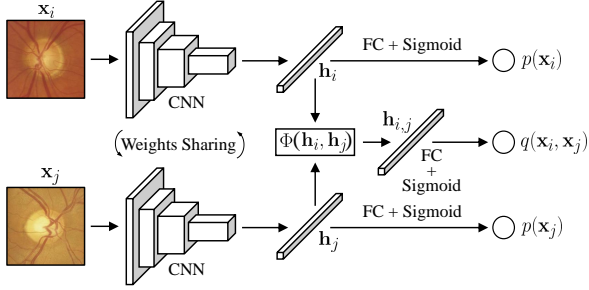


Figure 2: An illustration of our multi-task twin neural network for learning glaucoma diagnosis.

erative modeling [55]. Multi-task learning simultaneously learns multiple related tasks by exploiting task-generic and task-specific information [4]. Embedding learning learns a feature (embedding) \mathbf{h} from each image \mathbf{x} , as illustrated in Fig. 2, satisfying that the image features from the same class are closer in the embedding space, and vice versa [20]. Embedding learning algorithms are typically classified as either task-specific embedding models or task-invariant embedding models. The first group learns an embedding for each task, using the information only from that task, while the second category learns a general embedding with various outputs. Twin (or Siamese) neural network [24] is one of the most representative models of the second type. It is typically used for one/few/low-shot image, *e.g.*, face or digit, recognition. In Sec. 3.1 and 4.2.2, we explore the feasibility of learning glaucoma diagnosis using a MTTNN. Learning with external memory extracts prior knowledge from a low-shot training set and stores it in an external memory, such as a key-value memory [37]. Each test image is then predicted based on a weighted average of contents extracted from the memory. Our proposed OVV self-training strategy, as introduced in Sec. 3.2, is also motivated by the mechanism of learning with external memory, where the labels of unlabeled training data are predicted by a classifier trained on a collection of images in the low-shot training set. Finally, generative modeling algorithms aim at estimating the probability distribution from observed data with the help of prior knowledge, typically based on Bayes' theorem [27, 13].

2.3. Semi-Supervised Learning

In comparison to LSL that uses only a small amount of labeled data, SSL also includes a large amount of unlabeled data for training [5], as illustrated in Fig. 1. It falls between unsupervised learning and supervised learning. The most common taxonomy categorizes existing methods as either inductive or transductive [54]. The former requires a pre-trained model (typically yielded via supervised learning) to produce pseudo labels of the unlabeled data, while the latter does not require such a model to do so. Self-training [53] and co-training [2] are the two most popular inductive SSL

approaches. The essential distinction between them is the number of pretrained network(s) used to produce pseudo labels: self-training uses one, but co-training uses two. Developing an effective policy to identify confident predictions to produce pseudo labels is, therefore, the key to SSL. Moreover, preparing a reliable classifier with only a small amount of labeled data is notably demanding. Here, we combine SSL with LSL to biomedical image classification tasks, such as glaucoma diagnosis from fundus images.

3. Methodology

3.1. Multi-Task Twin Neural Network

As mentioned in Sec. 2.2, a twin neural network is a typical task-invariant embedding model, commonly utilized for metric learning and one/few/low-shot image recognition [24]. As its name implies, a twin neural network contains two identical sub-networks. A given pair of images \mathbf{x}_i and \mathbf{x}_j are separately fed into these sub-networks, which then output two 1D embeddings (features) \mathbf{h}_i and \mathbf{h}_j , respectively. $\Phi(\cdot)$ measures the distance between \mathbf{h}_i and \mathbf{h}_j by computing their vector absolute difference (AD) or squared difference (SD) $\mathbf{h}_{i,j}$, which is then followed by a fully connected (FC) layer to produce a scalar $q(\mathbf{x}_i, \mathbf{x}_j) \in [0, 1]$ indicating the similarity between \mathbf{x}_i and \mathbf{x}_j . When \mathbf{x}_i and \mathbf{x}_j are different, $q(\mathbf{x}_i, \mathbf{x}_j)$ approaches 1, and vice versa. $y_i \in \{0, 1\}$ and $y_j \in \{0, 1\}$ denote the ground truth labels of \mathbf{x}_i and \mathbf{x}_j , respectively, where 0 is healthy and 1 is glaucomatous optic neuropathy (GON).

However, such a twin neural network can only determine whether \mathbf{x}_i and \mathbf{x}_j belong to the same category, *i.e.*, healthy or GON, instead of predicting their independent categories. A straightforward solution is to separately connect \mathbf{h}_i and \mathbf{h}_j with a FC layer to produce the scalars $p(\mathbf{x}_i)$ and $p(\mathbf{x}_j)$ indicating the probabilities that \mathbf{x}_i and \mathbf{x}_j are GON, respectively. See Fig. 2 and note that the two FC layers use the same weights. In this paper, we refer to the CNN architecture in Fig. 2 as a MTTNN, which is capable of simultaneously classifying a given pair of fundus images into either healthy or GON as well as measuring their similarity. Using such a task-invariant embedding model, we can have $C(n, 2)$ different combinations of image pairs, where n represents the low-shot sample size. For example, the 1147 fundus images we used in our experiments can provide over 657K different pairs, which can overcome the small sample size issue and prevent overfitting.

In this paper, we use n_0 and n_1 to denote the numbers of healthy and GON fundus images, respectively, used for LSL. n_0 is usually much greater than n_1 , because there are fewer patients with glaucomatous disease than healthy patients, resulting in a severe dataset imbalance problem. In this regard, we apply two weights $\omega_{\text{cla}} = \frac{n_0}{n_0 + n_1}$ and $\omega_{\text{sim}} = \frac{n_0(n_0 - 1) + n_1(n_1 - 1)}{(n_0 + n_1)(n_0 + n_1 - 1)}$ to weigh the losses \mathcal{L}_{cla} and

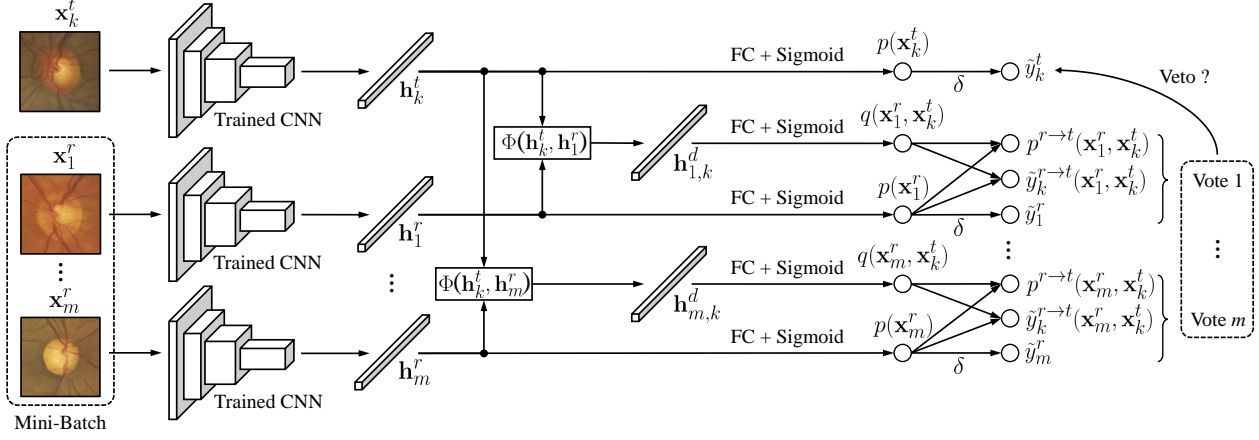


Figure 3: An illustration of our One-Vote Veto self-training strategy. $\mathbf{h}_{1,k}^d$ and $\mathbf{h}_{m,k}^d$ are two 1D embeddings, followed by a FC layer to produce scalars indicating the similarities between the given pairs of reference and target fundus images.

\mathcal{L}_{sim} , that are used for fundus image classification and input similarity measurement tasks, respectively. ω_{cla} represents the proportion of healthy fundus images in the training set, while ω_{sim} represents the proportion of the cases that the given labeled fundus image pairs $\mathbf{z} = [(\mathbf{x}_i, y_i), (\mathbf{x}_j, y_j)]$ belong to the same category. We train our MTTNN by minimizing a combined weighted (binary) cross-entropy loss, as follows:

$$\mathcal{L}(\mathbf{z}) = \lambda \mathcal{L}_{\text{cla}}(\mathbf{z}) + \mathcal{L}_{\text{sim}}(\mathbf{z}), \quad (1)$$

where

$$\begin{aligned} \mathcal{L}_{\text{cla}}(\mathbf{z}) = & - \left(\omega_{\text{cla}} (y_i \log(p(\mathbf{x}_i)) + y_j \log(p(\mathbf{x}_j))) \right. \\ & + (1 - \omega_{\text{cla}}) ((1 - y_i) \log(1 - p(\mathbf{x}_i)) \\ & \left. + (1 - y_j) \log(1 - p(\mathbf{x}_j))) \right), \end{aligned} \quad (2)$$

$$\begin{aligned} \mathcal{L}_{\text{sim}}(\mathbf{z}) = & - (\omega_{\text{sim}} |y_i - y_j| \log(q(\mathbf{x}_i, \mathbf{x}_j)) \\ & + (1 - \omega_{\text{sim}}) (1 - |y_i - y_j|) \log(1 - q(\mathbf{x}_i, \mathbf{x}_j))), \end{aligned} \quad (3)$$

λ is a hyper-parameter utilized to balance \mathcal{L}_{cla} and \mathcal{L}_{sim} ; The motivations of using such a combined weighed cross-entropy loss function to train our MTTNN, instead of the conventionally used triplet loss [17] or contrastive loss [23] are:

1. Most datasets for glaucoma diagnosis are imbalanced. As detailed in Sec. 4.1, the OHTS [14] training set is severely imbalanced (50208 healthy images vs. 2416 GON images for supervised learning, and 995 healthy images vs. 152 GON images for LSL). Learning from such an imbalanced dataset without weights on the different classes can result in many incorrect predictions (most GON images are likely to be predicted as healthy images). In this regard, different weights should be used for different classes (a higher weight should be

used for the minority class) so as to prevent CNN from predicting all the images as the majority class.

2. It is usually difficult to weigh different types of losses, *e.g.*, regression and classification, in multi-task learning [22]. An undesirable weight can result in a poorly-performing task, when other tasks converge to satisfactory results. Therefore, formulating \mathcal{L}_{sim} as a weighted cross-entropy loss function is a simple but effective solution. However, due to the dataset imbalance problem discussed above, ω_{sim} is included in (3).
3. As shown in Fig. 3, our proposed self-training strategy requires both labels and probabilities (of being GON images), predicted by a pretrained model, to produce pseudo labels of the unlabeled data. Such network architecture and training loss can efficiently and effectively provide both “self-predicted” and “contrastively-predicted” labels and probabilities, as explained in Sec. 3.2.

It should be noted here that the images from the same patient are not used as an image pair for MTTNN training. The selection of λ and $\Phi(\cdot)$ is discussed in Sec. 4.2.2.

3.2. One-Vote Veto Self-Training

As introduced in Sec. 2.3, self-training aims to improve the performance of a pretrained model, by incorporating confident predictions of the unlabeled data to obtain useful additional information that can be used during training. A feasible strategy to determine such confident predictions is, therefore, the key to self-training [34].

For conventional SSL algorithms, given a pretrained image classification model (through supervised learning), a straightforward way to determine whether an unlabeled image is confident enough to be included for model finetuning is to compare its probability distributed to the most possible class, with a predetermined threshold. If its probability exceeds that threshold, its prediction will be considered as

Algorithm 1: One-Vote Veto self-training strategy.

Data: \mathcal{X}^r , \mathcal{Y}^r , and \mathcal{X}^t

```
1 while Training do
2   Given a mini-batch consisting of
      $\{\mathbf{x}_1^r, \dots, \mathbf{x}_m^r\} \in \mathcal{X}^r$ ,  $\{y_1^r, \dots, y_m^r\} \in \mathcal{Y}^r$  and
      $\{\mathbf{x}_1^t, \dots, \mathbf{x}_m^t\} \in \mathcal{X}^t$ ;
3    $\mathcal{P} \leftarrow \emptyset$ ;
4   for  $i \leftarrow 1$  to  $m$  do
5     if  $|p(\mathbf{x}_i^t) - \frac{1}{2}| > \frac{1}{2} - \kappa_2$  then
6        $w \leftarrow 0$ ;
7       for  $j \leftarrow 1$  to  $m$  do
8         if  $|p(\mathbf{x}_j^r) - y_j^r| < \kappa_2$ 
9           then
10             $w \leftarrow w + 1$ ;
11             $\mathcal{P} \leftarrow \mathcal{P} \cup \{\mathbf{x}_j^r, y_j^r\}$ ;
12             $\mathbf{v}_1(j) \leftarrow \tilde{y}_i^{r \rightarrow t}(\mathbf{x}_j^r, \mathbf{x}_i^t)$ ;
13             $\mathbf{v}_2(j) \leftarrow p^{r \rightarrow t}(\mathbf{x}_j^r, \mathbf{x}_i^t)$ ;
14          if  $(\sum_{j=1}^m \mathbf{v}_1(j) \leq \kappa_1 \vee \sum_{j=1}^m \mathbf{v}_2(j) \geq w - \kappa_1)$ 
15             $\wedge$  any  $|\mathbf{v}_2(j) - \frac{1}{2}| > \frac{1}{2} - \kappa_2$ 
16            then
17               $\mathcal{P} \leftarrow \mathcal{P} \cup \{\mathbf{x}_i^t, \tilde{y}_i^t\}$ 
18  finetune the target model using  $\mathcal{P}$ ;
19  if the target model outperforms the reference model then
20    Update the reference model parameters;
```

a pseudo label. The image and its pseudo label will then be incorporated into the labeled data to finetune the pretrained model.

However, relying on probability distributions alone to generate pseudo labels is not often sufficient [53]. Inspired by learning with external memory [45], we introduce OVV self-training in this paper, as illustrated in Fig. 3. Similar to learning with external memory [45], we use a collection of m reference (labeled) fundus images $\{\mathbf{x}_1^r, \dots, \mathbf{x}_m^r\} \in \mathcal{X}^r$ to provide “contrastive predictions” to the target (unlabeled) fundus images $\{\mathbf{x}_1^t, \dots, \mathbf{x}_m^t\} \in \mathcal{X}^t$, where the superscripts r and t represent “reference” and “target”, respectively. The contrastive predictions then vote to veto the unconfident “self-predictions” $\{\tilde{y}_1^t, \dots, \tilde{y}_m^t\}$ produced by the MTTNN. Our OVV self-training algorithm is detailed in Algorithm 1, where the target model updates its parameters during self-training but the reference model does not.

When finetuning a MTTNN pretrained through LSL, each mini-batch contains a discrete set of m reference fundus images $\{\mathbf{x}_1^r, \dots, \mathbf{x}_m^r\} \in \mathcal{X}^r$, their ground truth labels $\{y_1^r, \dots, y_m^r\} \in \mathcal{Y}^r$, and the same number of m target fundus images $\{\mathbf{x}_1^t, \dots, \mathbf{x}_m^t\} \in \mathcal{X}^t$ without labels. \mathbf{h}_k^r and \mathbf{h}_k^t represent the 1D embeddings learned from \mathbf{x}_k^r and \mathbf{x}_k^t ($k \in [1, m] \cap \mathbb{Z}$), respectively. Given a pair of reference and target fundus images, \mathbf{x}_q^r and \mathbf{x}_k^t , the pretrained MTTNN can “self-predict” both the scalars $p(\mathbf{x}_q^r)$ and $p(\mathbf{x}_k^t)$ which indicate the probabilities that \mathbf{x}_q^r and \mathbf{x}_k^t are GON, respectively, as well as their labels $\tilde{y}_q^r = \delta(p(\mathbf{x}_q^r))$ and

$\tilde{y}_k^t = \delta(p(\mathbf{x}_k^t))$ using its fundus image classification functionality ($\delta(p) = 1$ when $p > 0.5$, and $\delta(p) = 0$ otherwise). $p(\mathbf{x}_q^r)$ is then used to determine whether \mathbf{x}_q^r is qualified to veto unconfident predictions. In the mean time, the pre-trained MTTNN can also “contrastively-predict” the scalar

$$p^{r \rightarrow t}(\mathbf{x}_q^r, \mathbf{x}_k^t) = |p(\mathbf{x}_q^r) - q(\mathbf{x}_q^r, \mathbf{x}_k^t)| \quad (4)$$

indicating the GON probability as well as the label

$$\tilde{y}_k^{r \rightarrow t}(\mathbf{x}_q^r, \mathbf{x}_k^t) = |\delta(p(\mathbf{x}_q^r)) - \delta(q(\mathbf{x}_q^r, \mathbf{x}_k^t))| \quad (5)$$

of \mathbf{x}_k^t from \mathbf{x}_q^r using its input similarity measurement functionality. **Please note:** $\tilde{y}_k^{r \rightarrow t}(\mathbf{x}_q^r, \mathbf{x}_k^t)$ is typically unequal to $\delta(p^{r \rightarrow t}(\mathbf{x}_q^r, \mathbf{x}_k^t))$. In order to determine whether \tilde{y}_k^t is confident and can be used as the pseudo label of \mathbf{x}_k^t , all the reference fundus images $\{\mathbf{x}_1^r, \dots, \mathbf{x}_m^r\} \in \mathcal{X}^r$ in the mini-batch are used to provide additional judgements. Each pair of contrastively-predicted scalar indicating GON probability and label form a vote ($p^{r \rightarrow t}(\mathbf{x}_q^r, \mathbf{x}_k^t), \tilde{y}_k^{r \rightarrow t}(\mathbf{x}_q^r, \mathbf{x}_k^t)$). If $|p(\mathbf{x}_q^r) - y_q^r| > \kappa_2$, we will omit its vote, where κ_2 is a threshold used to select qualified reference fundus images.

With all votes collected from the qualified reference fundus images, the OVV self-training algorithm determines whether \tilde{y}_k^t should be used as the pseudo label for \mathbf{x}_k^t based on the following criteria:

- Identical to the manner of determining qualified reference fundus images, if any $p^{r \rightarrow t}(\mathbf{x}_j^r, \mathbf{x}_k^t)$ ($j \in [1, m] \cap \mathbb{Z}$) or $p(\mathbf{x}_k^t)$ is not close to either 0 (healthy) or 1 (GON), evaluated by the threshold κ_2 , \tilde{y}_k^t will not be assigned to \mathbf{x}_k^t .
- If a minority of more than κ_1 qualified reference fundus images disagree with the majority of the qualified reference fundus images, \tilde{y}_k^t will not be assigned to \mathbf{x}_k^t .

As discussed in Sec. 4.2.2, $\kappa_1 = 0$ (all the qualified reference images vote to the same category) achieves the best overall performance. In this regard, the above-mentioned strategy is referred to “One-Vote Veto” in this paper. Since each target fundus image is required to be compared with all the reference fundus images in the same mini-batch, the proposed self-training strategy has a computational complexity of $\mathcal{O}(n^2)$, which is relatively memory-consuming. The confident target fundus images and their pseudo labels are then included into the low-shot data to finetune the pretrained MTTNN with supervised learning by minimizing a weighted cross-entropy loss. The OVV performance with respect to different κ_1, κ_2 and m is also shown in Sec. 4.2.2.

4. Experimental Results

4.1. Datasets and Experimental Setups

The datasets used in our experiments were collected at various intervals by different clinicians from different institutes using different fundus cameras. Their details are as follows:

- **OHTS:** The OHTS [15, 21, 14] recruited 1636 ocular hypertensive participants with elevated intraocular pressure [14]. The OHTS [14] dataset utilized in our experiments contains 66715 raw fundus images. In our experiments, a square region centered on the optic nerve head (ONH) was first extracted from each raw fundus image using a well-trained DeepLabv3+ [7] model. A small part of the raw data are stereoscopic fundus images, each of which was split to produce two individual fundus images. This image preprocessing resulted in a total number of 74768 fundus images. Moreover, ENPOAGDISC (endpoint committee attributable to primary open angle glaucoma based on optic disc changes from photographs) labels are used as the classification ground truth. The total number of fundus images are divided into a training set (50208 healthy images and 2416 GON images), a validation set (7188 healthy images and 426 GON images), and an independent test set (13780 healthy images and 792 GON images) **by participant**. Additionally, we select one image from each patient in the training set to create the low-shot training set (995 healthy images and 152 GON images). **Please note: all images from each patient are in only one of these three subsets.**
- **ACRIMA:** The ACRIMA [11] dataset consists of 309 healthy images and 396 GON images. It was collected as part of an initiative by the government of Spain. Classification was based on review by a single experienced glaucoma expert. Images were excluded if they did not provide a clear view of the ONH region [9].
- **LAG:** The LAG [28] dataset contains 3143 healthy images and 1711 GON images¹, obtained from Beijing Tongren Hospital. Similar to the OHTS [14] dataset, we also use the well-trained DeepLabv3+ [7] model to extract a square region centered on the ONH from each fundus image.
- **DIGS/ADAGES:** The UCSD-based Diagnostic Innovations in Glaucoma Study (DIGS) and African Descent and Glaucoma Evaluation Study (ADAGES) [41] are longitudinal studies designed to detect and monitor glaucoma based on optical imaging and visual function testing that, when combined, have generated tens of thousands of test results from over 4000 healthy, glaucoma suspect or glaucoma eyes over the course of up to 25 years. In our experiments, we use the DIGS/ADAGES [41] test set to evaluate the performance of our proposed methods. It contains 5184 healthy images and 4289 GON images.

The aforementioned four test sets are visualized with t-SNE [32], as shown in Fig. 4. Since healthy and GON images are distributed similarly between the OHTS [14]

¹The number of fundus images being published is fewer than what was reported in publication [28].

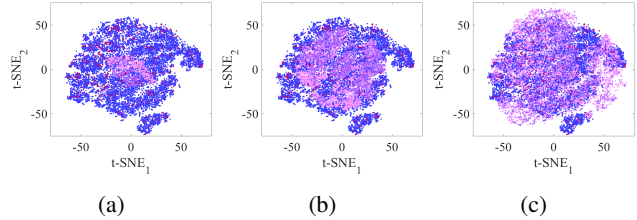


Figure 4: Comparison of dataset visualization produced by t-SNE [32], where \bullet and \bullet represent the healthy and GON images in the OHTS [14] test set, respectively; \bullet and \bullet in (a) represent the healthy and GON images in the ACRIMA [11] dataset, respectively; \bullet and \bullet in (b) represent the healthy and GON images in the LAG [28] dataset, respectively; \bullet and \bullet in (c) represent the healthy and GON images in the DIGS/ADAGES [41] dataset, respectively.

and LAG [28] datasets, we expect models to perform similarly on these data. Dissimilar distribution in the ACRIMA [11] dataset led us to believe the performance of models in this dataset would be somewhat worse. Using these four datasets, we conduct three experiments:

- **Supervised learning experiment:** we utilize transfer learning [48] to train ResNet-50 [16] and MobileNet-v2 [42] (pretrained on the ImageNet database [10]), on the entire OHTS [14] training set. The best-performing models of these two CNNs are selected using the OHTS [14] validation set. Their performances are evaluated on the OHTS [14] test set, the ACRIMA [11] dataset, the LAG [28] dataset, and the DIGS/ADAGES [41] test set.
- **LSL experiment:** ResNet-50 [16] and MobileNet-v2 [42] (pretrained on the ImageNet database [10]) are separately used as the backbone CNNs of the MTTNN, introduced in Sec. 3.1. The corresponding MTTNNs are referred to as **ResNet-50-LS** and **MobileNet-v2-LS**, respectively. These MTTNNs are subsequently trained on the OHTS [14] low-shot training set. The validation and testing procedures are identical to those in the supervised learning experiment.
- **SSL experiment:** the well-trained ResNet-50-LS and MobileNet-v2-LS are finetuned on the entire OHTS [14] training set, but only the fundus images in the OHTS [14] low-shot training set have ground-truth labels. The finetuned ResNet-50-LS and MobileNet-v2-LS are referred to as **ResNet-50-OVV** and **MobileNet-v2-OVV**, respectively. The validation and testing procedures are identical to those in the supervised learning experiment.

The fundus images are resized to 224×224 pixels. The initial learning rate is set to 0.001, which decays gradually after the 100th epochs. Due to the dataset imbalance problem, F-score is utilized to select the best-performing models during the validation stage. Moreover, we adopt

Network	Training method	OHTS [14]	ACRIMA [11]	LAG [28]	DIGS/ADAGES [41]	t (min)
ResNet-50 [16]	Supervised learning	0.904 (95% CI: 0.865, 0.935)	0.736 (95% CI: 0.698, 0.771)	0.794 (95% CI: 0.780, 0.807)	0.744 (95% CI: 0.696, 0.792)	52.1
ResNet-50-LS (ours)	Low-shot learning	0.869 (95% CI: 0.833, 0.901)	0.758 (95% CI: 0.723, 0.792)	0.841 (95% CI: 0.829, 0.853)	0.743 (95% CI: 0.683, 0.795)	1.8
ResNet-50-OVV (ours)	Semi-supervised learning	0.898 (95% CI: 0.857, 0.928)	0.775 (95% CI: 0.741, 0.808)	0.881 (95% CI: 0.870, 0.891)	0.763 (95% CI: 0.695, 0.820)	203.7
MobileNet-v2 [42]	Supervised learning	0.893 (95% CI: 0.845, 0.932)	0.794 (95% CI: 0.760, 0.825)	0.856 (95% CI: 0.844, 0.867)	0.786 (95% CI: 0.728, 0.835)	42.9
MobileNet-v2-LS (ours)	Low-shot learning	0.859 (95% CI: 0.813, 0.896)	0.820 (95% CI: 0.786, 0.850)	0.843 (95% CI: 0.831, 0.855)	0.748 (95% CI: 0.689, 0.802)	1.2
MobileNet-v2-OVV (ours)	Semi-supervised learning	0.887 (95% CI: 0.850, 0.920)	0.840 (95% CI: 0.808, 0.867)	0.851 (95% CI: 0.838, 0.862)	0.777 (95% CI: 0.718, 0.826)	125.4

Table 1: AUC (shown along with 95% CI) and training time per epoch t (min) of supervised learning, low-shot learning and semi-supervised learning for glaucoma diagnosis. These results suggest that OVV strategy that requires a smaller sample size of labeled images performs similarly and in some cases significantly better than the backbone CNNs trained with a larger number of labeled images under full supervision.

an early stopping mechanism during the validation stage to reduce the overfitting problem, namely, the training will be terminated if the achieved F-score has not increased for 30 epochs. In addition, we use four metrics: 1) accuracy (ACC), 2) F-score, 3) Matthews correlation coefficient (MCC), and 4) AUC to quantify the performances of the trained models. Additional performance evaluation with more details is also provided in our supplementary material.

4.2. Performance Evaluation

4.2.1 Performance comparison of supervised learning, LSL, and SSL for glaucoma diagnosis

The comparisons of supervised learning, LSL, and SSL for glaucoma diagnosis are provided in Tab. 1.

First, these results suggest that our OVV self-training strategy that requires a smaller sample size of labeled images performs similarly (AUC 95% CI overlaps considerably) and, in some cases, significantly better (AUC 95% CI does not overlap) than the backbone CNNs trained with a larger number of labeled images under full supervision. Specifically, ResNet-50-OVV performs similarly to ResNet-50 [16] on the DIGS/ADAGES [41] test set, with AUC (95% CI) of 0.763 (0.695, 0.820) and 0.744 (0.696, 0.792), respectively, on the OHTS [14] test set, with AUC (95% CI) of 0.898 (0.857, 0.928) and 0.904 (0.865, 0.935), respectively, and on the ACRIMA [11] test set, with AUC (95% CI) of 0.775 (0.741, 0.808) and 0.736 (0.698, 0.771), respectively. ResNet-50-OVV performs significantly better on the LAG [28] dataset than ResNet-50 [16] with AUC (95% CI) of 0.881 (0.870, 0.891) and 0.794 (0.780, 0.807), respectively. MobileNet-v2-OVV also performs similarly to MobileNet-v2 [42] on all the four test sets.

Second as expected, the AUC scores achieved by LSL are in most, but not all, cases slightly lower than those achieved by the backbone CNNs on the OHTS [14] test set (~ 0.035 for ResNet-50 [16] and ~ 0.036 for MobileNet-v2 [42]). Moreover, since our LSL uses only a small amount of training data, MTTNN training is much faster than supervised learning.

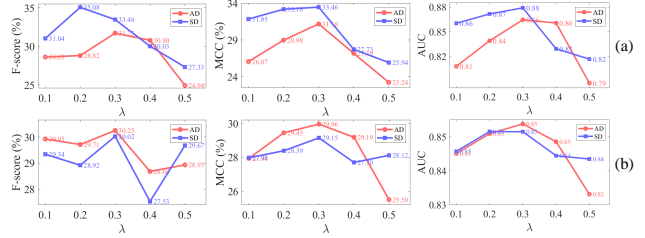


Figure 5: λ selection: (a) ResNet-50-LS results and (b) MobileNet-v2-LS results suggest that when $\lambda = 0.3$, LSL performs best.

4.2.2 Hyper-Parameter and Threshold Selection

We next discuss the selection of λ and $\Phi(\cdot)$. In our experiments, we set λ to 0.1, 0.2, 0.3, 0.4 and 0.5 respectively, and compare the MTTNN performance when $\Phi(\cdot)$ performs AD and SD. The comparisons in terms of F-score, MCC and AUC on the OHTS [14] test set are provided in Fig. 5, where ResNet-50-LS-AD and MobileNet-v2-LS-AD perform AD in $\Phi(\cdot)$, while ResNet-50-LS-SD and MobileNet-v2-LS-SD perform SD in $\Phi(\cdot)$, respectively. From Fig. 5, it is obvious that when $\lambda = 0.3$, the MTTNN achieves the best overall performance, which is reasonable, as a higher λ weighs more on the image classification task, easily resulting in overfitting. Also, ResNet-50-LS-SD typically outperforms ResNet-50-LS-AD while MobileNet-v2-LS-AD typically outperforms MobileNet-v2-LS-SD. To determine the generalizability of the trained models, we further evaluate them on three additional datasets, as shown in Tab. 2. Compared with SD, when $\Phi(\cdot)$ applies AD, MTTNN generally performs better or very similarly on the additional test sets, especially for ResNet-50-LS on the ACRIMA [11] dataset. AD is therefore used in the following experiments. Furthermore, Tab. 2 shows a baseline supervised learning experiment with the low-shot training set. The results suggest that LSL performs much better than its backbone CNN (trained with supervised learning) when the training size is small.

Furthermore, we discuss the selection of the thresholds κ_1 and κ_2 used in OVV self-training as well as the impact of different mini-batch size $2m$ on the performance of OVV self-training. Tab. 3 provides the performances of ResNet-50-OVV and MobileNet-v2-OVV with respect to different κ_1 , κ_2 and m . It can be seen that the ACC and F-score increase slightly but the MCC and AUC almost remain the

Test set	Network	ACC (%)	F-score (%)	MCC (%)	AUC
ACRIMA [11]	ResNet-50 [16]	57.163	56.734	16.387	0.625
	ResNet-50-LS-AD	67.092	63.175	41.015	0.758
	ResNet-50-LS-SD	49.504	25.523	13.322	0.437
LAG [28]	ResNet-50 [16]	64.318	57.445	29.116	0.714
	ResNet-50-LS-AD	79.028	65.908	52.381	0.841
	ResNet-50-LS-SD	78.039	68.179	51.452	0.826
DIGS/ ADAGES [41]	ResNet-50 [16]	59.639	59.708	19.674	0.648
	ResNet-50-LS-AD	67.745	60.754	35.505	0.743
	ResNet-50-LS-SD	65.736	55.722	31.918	0.700

(a)

Dataset	Network	ACC (%)	F-score (%)	MCC (%)	AUC
ACRIMA [11]	MobileNet-v2 [42]	73.333	78.341	45.505	0.779
	MobileNet-v2-LS-AD	70.355	67.797	46.421	0.820
	MobileNet-v2-LS-SD	66.241	59.107	43.800	0.823
LAG [28]	MobileNet-v2 [42]	65.122	63.268	38.373	0.781
	MobileNet-v2-LS-AD	79.007	69.482	53.536	0.843
	MobileNet-v2-LS-SD	78.430	61.830	51.035	0.846
DIGS/ ADAGES [41]	MobileNet-v2 [42]	61.478	66.128	26.319	0.669
	MobileNet-v2-LS-AD	69.176	68.145	38.363	0.748
	MobileNet-v2-LS-SD	68.120	64.028	35.869	0.740

(b)

Table 2: Supervised learning of backbone network with small sample size vs. LSL: ResNet-50 [16] and MobileNet-v2 [42] are trained using supervised learning on the OHTS [14] low-shot training set. ResNet-50-LS-AD/SD and MobileNet-v2-LS-AD/SD are trained using LSL. λ is set to 0.3. The best results are shown in bold font. These results suggest that in the small sample case, LSL improves the performance of the backbone CNNs.

Network	κ_1	κ_2	m	ACC (%)	F-score (%)	MCC (%)	AUC	
ResNet-50-OVV	0	0.01	20	91.415 \uparrow	41.148 \uparrow	39.875 \uparrow	0.898 \uparrow	
	0	0.01	15	92.113 \uparrow	41.316 \uparrow	39.341 \uparrow	0.898 \uparrow	
	0	0.01	10	94.199 \uparrow	43.759 \uparrow	40.831 \uparrow	0.890 \uparrow	
	0	0.1	20	90.516 \uparrow	38.139 \uparrow	36.874 \uparrow	0.898 \uparrow	
	2	0.01	20	90.717 \uparrow	35.818 \uparrow	33.686 \uparrow	0.885 \uparrow	
	2	0.1	20	92.656 \uparrow	32.017 \uparrow	28.390 \downarrow	0.851 \downarrow	
	4	0.01	20	92.610 \uparrow	29.668 \downarrow	25.911 \downarrow	0.854 \downarrow	
	4	0.1	20	92.672 \uparrow	28.463 \downarrow	24.675 \downarrow	0.842 \downarrow	
	MobileNet-v2-OVV	0	0.01	25	90.609 \uparrow	36.960 \uparrow	35.240 \uparrow	0.887 \uparrow
		0	0.01	20	93.470 \uparrow	36.976 \uparrow	33.658 \uparrow	0.893 \uparrow
		0	0.01	15	93.742 \uparrow	37.779 \uparrow	34.535 \uparrow	0.863 \uparrow
		0	0.1	25	88.825 \uparrow	34.351 \uparrow	33.401 \uparrow	0.878 \uparrow
2		0.01	25	93.463 \uparrow	35.204 \uparrow	31.814 \uparrow	0.862 \uparrow	
2		0.1	25	90.772 \uparrow	32.616 \uparrow	29.701 \downarrow	0.858 \uparrow	
2		0.01	25	92.268 \uparrow	31.852 \uparrow	28.242 \downarrow	0.854 \uparrow	
2		0.1	25	90.803 \uparrow	32.690 \uparrow	29.772 \downarrow	0.859 \uparrow	

Table 3: Evaluation of the OVV self-training on the OHTS [14] test set with respect to different κ_1 , κ_2 and m , where ResNet-50-OVV finetunes ResNet-50-LS, and MobileNet-v2-OVV finetunes MobileNet-v2-LS. The best results are shown in bold font. \uparrow indicates SSL outperforms LSL.

same, with the decrease of m . Moreover, with the increase of κ_1 and κ_2 , the standard to determine confident predictions becomes lower, which makes the SSL performance degrade. It should be noted here that when $\kappa_1 \neq 0$, our self-training strategy should not be named as ‘‘One-Vote Veto’’, as mentioned in Sec. 3.2. Based on this experiment, we believe OVV self-training benefits from smaller κ_1 and κ_2 .

Additionally, ResNet-50-OVV and MobileNet-v2-OVV, trained under different m , are also tested on the three additional test sets, as shown in Tab. 4. It can be seen that the network trained under a larger m typically shows

Dataset	m	ACC (%)	F-score (%)	MCC (%)	AUC
ACRIMA [11]	20	59.858 \downarrow	49.192 \downarrow	31.712 \downarrow	0.775 \uparrow
	15	60.426 \downarrow	49.365 \downarrow	33.779 \downarrow	0.751 \downarrow
	10	54.610 \downarrow	35.743 \downarrow	25.766 \downarrow	0.721 \downarrow
LAG [28]	20	80.882 \uparrow	66.304 \uparrow	57.255 \uparrow	0.881 \uparrow
	15	76.864 \downarrow	56.252 \downarrow	47.552 \downarrow	0.825 \downarrow
	10	76.638 \downarrow	56.518 \downarrow	46.753 \downarrow	0.826 \downarrow
DIGS/ADAGES [41]	20	67.813 \uparrow	58.315 \uparrow	36.490 \uparrow	0.763 \uparrow
	15	63.045 \downarrow	44.727 \downarrow	28.607 \downarrow	0.753 \uparrow
	10	61.819 \downarrow	41.340 \downarrow	26.202 \downarrow	0.727 \downarrow

(a)

Dataset	m	ACC (%)	F-score (%)	MCC (%)	AUC
ACRIMA [11]	25	72.340 \uparrow	70.229 \uparrow	50.119 \uparrow	0.840 \uparrow
	20	63.404 \downarrow	54.895 \downarrow	38.402 \downarrow	0.814 \downarrow
	15	61.986 \downarrow	51.273 \downarrow	37.706 \downarrow	0.826 \uparrow
LAG [28]	25	79.625 \uparrow	65.262 \uparrow	53.834 \uparrow	0.851 \uparrow
	20	76.670 \downarrow	55.906 \downarrow	47.109 \downarrow	0.841 \downarrow
	15	75.834 \downarrow	51.748 \downarrow	45.522 \downarrow	0.866 \uparrow
DIGS/ADAGES [41]	25	69.653 \uparrow	63.258 \downarrow	39.454 \uparrow	0.777 \uparrow
	20	66.383 \downarrow	52.888 \downarrow	34.960 \downarrow	0.773 \uparrow
	15	63.965 \downarrow	44.198 \downarrow	32.099 \downarrow	0.789 \uparrow

(b)

Table 4: The evaluation of OVV self-training with respect to different m on the additional test sets: (a) ResNet-50-OVV and (b) MobileNet-v2-OVV. The best results are shown in bold font. \uparrow indicates SSL outperforms LSL.

better results. When m decreases, the generalizability of MTTNN degrades dramatically, especially for F-score (decreases by around 9-19%) and MCC (decreases by around 6-12%). Therefore, increasing the mini-batch size can improve the MTTNN generalizability, as more reference fundus images are used to provide contrastive-predictions for the target fundus images, which can veto more unconfident predictions on the unlabeled data. Since our threshold selection experiments cover a very limited number of discrete sets of κ_1 , κ_2 , and m , we believe better performance can be achieved when more values are tested.

5. Conclusion

The main contributions of this paper include: 1) a multi-task twin neural network that can learn glaucoma diagnosis from very limited labeled training data; 2) an effective semi-supervised learning strategy, referred to as One-Vote Veto self-training, which is designed specially for low-shot learning of task-invariant embeddings to diagnose glaucoma. Extensive experiments conducted on four glaucoma datasets demonstrated the effectiveness of the aforementioned techniques, where the AUC achieved by low-shot learning is only slightly lower than that produced by the backbone CNN trained under full supervision. In addition, with One-Vote Veto self-training, the multi-task twin neural networks perform similarly to their backbone CNNs on the OHTS [14] test set but show better generalization performances on three additional test sets. With more thresholds and hyper-parameters being tested, we believe our proposed One-Vote Veto self-training strategy for low-shot learning of task-invariant embeddings can yield better overall performance. The techniques introduced in this paper also pro-

vide the potential to be applied for other binary biomedical image classification applications, which often suffer from small sample size issues with class imbalance.

References

- [1] Vijay Badrinarayanan, Alex Kendall, and Roberto Cipolla. Segnet: A deep convolutional encoder-decoder architecture for image segmentation. *IEEE transactions on pattern analysis and machine intelligence*, 39(12):2481–2495, 2017. [11](#), [12](#)
- [2] Avrim Blum and Tom Mitchell. Combining labeled and unlabeled data with co-training. In *Proceedings of the eleventh annual conference on Computational learning theory*, pages 92–100, 1998. [3](#)
- [3] Enrique J Carmona, Mariano Rincón, Julián García-Feijóo, and José M Martínez-de-la Casa. Identification of the optic nerve head with genetic algorithms. *Artificial Intelligence in Medicine*, 43(3):243–259, 2008. [14](#)
- [4] Rich Caruana. Multitask learning. *Machine learning*, 28(1):41–75, 1997. [3](#)
- [5] Olivier Chapelle, Bernhard Scholkopf, and Alexander Zien. Semi-supervised learning (chapelle, o. et al., eds.; 2006)[book reviews]. *IEEE Transactions on Neural Networks*, 20(3):542–542, 2009. [3](#)
- [6] Aditya Chattopadhyay, Anirban Sarkar, Prantik Howlader, and Vineeth N Balasubramanian. Grad-cam++: Generalized gradient-based visual explanations for deep convolutional networks. In *2018 IEEE Winter Conference on Applications of Computer Vision (WACV)*, pages 839–847. IEEE, 2018. [14](#)
- [7] Liang-Chieh Chen, Yukun Zhu, George Papandreou, Florian Schroff, and Hartwig Adam. Encoder-decoder with atrous separable convolution for semantic image segmentation. In *Proceedings of the European conference on computer vision (ECCV)*, pages 801–818, 2018. [6](#), [11](#), [12](#), [14](#)
- [8] Mark Christopher, Akram Belghith, Christopher Bowd, James A Proudfoot, Michael H Goldbaum, Robert N Weinreb, Christopher A Girkin, Jeffrey M Liebmann, and Linda M Zangwill. Performance of deep learning architectures and transfer learning for detecting glaucomatous optic neuropathy in fundus photographs. *Scientific reports*, 8(1):1–13, 2018. [2](#), [14](#)
- [9] Mark Christopher, Kenichi Nakahara, Christopher Bowd, James A Proudfoot, Akram Belghith, Michael H Goldbaum, Jasmin Rezapour, Robert N Weinreb, Massimo A Fazio, Christopher A Girkin, et al. Effects of study population, labeling and training on glaucoma detection using deep learning algorithms. *Translational Vision Science & Technology*, 9(2):27–27, 2020. [2](#), [6](#)
- [10] J. Deng, W. Dong, R. Socher, L.-J. Li, K. Li, and L. Fei-Fei. ImageNet: A Large-Scale Hierarchical Image Database. In *CVPR09*, 2009. [6](#)
- [11] Andrés Díaz Pinto, Sandra Morales Martínez, Valeriana Naranjo Ornedo, Thomas Köhler, José Manuel Mossi García, Amparo Navea Tejerina, et al. Cnns for automatic glaucoma assessment using fundus images: an extensive validation/andres diaz-pinto...[et al.]. *BioMedical Engineering OnLine*, vol. 18 (20 mar. 2019)., 2019. [6](#), [7](#), [8](#), [12](#), [13](#), [14](#)
- [12] Francisco Fumero, Silvia Alayón, José L Sanchez, Jose Sigut, and M Gonzalez-Hernandez. Rim-one: An open retinal image database for optic nerve evaluation. In *2011 24th international symposium on computer-based medical systems (CBMS)*, pages 1–6. IEEE, 2011. [14](#)
- [13] Jonathan Gordon, John Bronskill, Matthias Bauer, Sebastian Nowozin, and Richard Turner. Meta-learning probabilistic inference for prediction. In *International Conference on Learning Representations*, 2018. [3](#)
- [14] Mae O Gordon, Eve J Higginbotham, Dale K Heuer, Richard K Parrish II, Alan L Robin, Patricia A Morris, Deborah A Dunn, Bradley S Wilson, Michael A Kass, and Ocular Hypertension Treatment Study. Assessment of the impact of an endpoint committee in the ocular hypertension treatment study. *American journal of ophthalmology*, 199:193–199, 2019. [1](#), [2](#), [4](#), [6](#), [7](#), [8](#), [12](#), [13](#), [14](#)
- [15] Mae O Gordon and Michael A Kass. The ocular hypertension treatment study: design and baseline description of the participants. *Archives of Ophthalmology*, 117(5):573–583, 1999. [1](#), [2](#), [6](#)
- [16] Kaiming He, Xiangyu Zhang, Shaoqing Ren, and Jian Sun. Deep residual learning for image recognition. In *Proceedings of the IEEE conference on computer vision and pattern recognition*, pages 770–778, 2016. [2](#), [6](#), [7](#), [8](#), [12](#), [13](#), [14](#)
- [17] Elad Hoffer and Nir Ailon. Deep metric learning using triplet network. In *International Workshop on Similarity-Based Pattern Recognition*, pages 84–92. Springer, 2015. [4](#)
- [18] Wenbin Huang, Kai Gao, Yaoming Liu, Mengyin Liang, and Xiulan Zhang. The adverse impact of glaucoma on psychological function and daily physical activity. *Journal of Ophthalmology*, 2020, 2020. [1](#)
- [19] Devesh Jain, Tristan Swedish, Bailey Shen, David Y Kim, Shizuo Mukai, and Ramesh Raskar. Open-source, ultra-low-cost smartphone attachment for non-mydriatic fundus photography-open indirect ophthalmoscope. *Investigative Ophthalmology & Visual Science*, 57(12):1685–1685, 2016. [2](#)
- [20] Yangqing Jia, Evan Shelhamer, Jeff Donahue, Sergey Karayev, Jonathan Long, Ross Girshick, Sergio Guadarrama, and Trevor Darrell. Caffe: Convolutional architecture for fast feature embedding. In *Proceedings of the 22nd ACM international conference on Multimedia*, pages 675–678, 2014. [3](#)
- [21] Michael A Kass, Dale K Heuer, Eve J Higginbotham, Chris A Johnson, John L Keltner, J Philip Miller, Richard K Parrish, M Roy Wilson, and Mae O Gordon. The ocular hypertension treatment study: a randomized trial determines that topical ocular hypotensive medication delays or prevents the onset of primary open-angle glaucoma. *Archives of ophthalmology*, 120(6):701–713, 2002. [1](#), [2](#), [6](#)
- [22] Alex Kendall, Yarin Gal, and Roberto Cipolla. Multi-task learning using uncertainty to weigh losses for scene geometry and semantics. In *Proceedings of the IEEE conference on computer vision and pattern recognition*, pages 7482–7491, 2018. [4](#)

- [23] Prannay Khosla, Piotr Teterwak, Chen Wang, Aaron Sarna, Yonglong Tian, Phillip Isola, Aaron Maschinot, Ce Liu, and Dilip Krishnan. Supervised contrastive learning. *arXiv preprint arXiv:2004.11362*, 2020. [4](#)
- [24] Gregory Koch, Richard Zemel, and Ruslan Salakhutdinov. Siamese neural networks for one-shot image recognition. In *ICML deep learning workshop*, volume 2. Lille, 2015. [3](#)
- [25] Alex Krizhevsky. One weird trick for parallelizing convolutional neural networks. *arXiv preprint arXiv:1404.5997*, 2014. [2](#)
- [26] MiYoung Kwon, Carrie Huisingh, Lindsay A Rhodes, Gerald McGwin Jr, Joanne M Wood, and Cynthia Owsley. Association between glaucoma and at-fault motor vehicle collision involvement among older drivers: a population-based study. *Ophthalmology*, 123(1):109–116, 2016. [1](#)
- [27] Brenden M Lake, Ruslan Salakhutdinov, and Joshua B Tenenbaum. Human-level concept learning through probabilistic program induction. *Science*, 350(6266):1332–1338, 2015. [3](#)
- [28] Liu Li, Mai Xu, Xiaofei Wang, Lai Jiang, and Hanruo Liu. Attention based glaucoma detection: A large-scale database and cnn model. In *Proceedings of the IEEE Conference on Computer Vision and Pattern Recognition*, pages 10571–10580, 2019. [1](#), [6](#), [7](#), [8](#), [12](#), [13](#), [14](#)
- [29] Sidong Liu, Stuart L Graham, Angela Schulz, Michael Kalloniatis, Barbara Zangerl, Weidong Cai, Yang Gao, Brian Chua, Hemamalini Arvind, John Grigg, et al. A deep learning-based algorithm identifies glaucomatous discs using monoscopic fundus photographs. *Ophthalmology Glaucoma*, 1(1):15–22, 2018. [2](#)
- [30] Jonathan Long, Evan Shelhamer, and Trevor Darrell. Fully convolutional networks for semantic segmentation. In *Proceedings of the IEEE conference on computer vision and pattern recognition*, pages 3431–3440, 2015. [11](#), [12](#)
- [31] Ningning Ma, Xiangyu Zhang, Hai-Tao Zheng, and Jian Sun. Shufflenet v2: Practical guidelines for efficient cnn architecture design. In *Proceedings of the European conference on computer vision (ECCV)*, pages 116–131, 2018. [2](#)
- [32] Laurens van der Maaten and Geoffrey Hinton. Visualizing data using t-sne. *Journal of machine learning research*, 9(Nov):2579–2605, 2008. [6](#)
- [33] Everett matthew Lawson and Ramesh Raskar. Smart phone administered fundus imaging without additional imaging optics. *Investigative Ophthalmology & Visual Science*, 55(13):1609–1609, 2014. [2](#)
- [34] David McClosky, Eugene Charniak, and Mark Johnson. Effective self-training for parsing. In *Proceedings of the Human Language Technology Conference of the NAACL, Main Conference*, pages 152–159, 2006. [4](#)
- [35] Gerald McGwin Jr, Carrie Huisingh, Shelly Gupta Jain, Christopher A Girkin, and Cynthia Owsley. Binocular visual field impairment in glaucoma and at-fault motor vehicle collisions. *Journal of glaucoma*, 24(2):138, 2015. [1](#)
- [36] Felipe A Medeiros, Alessandro A Jammal, and Eduardo B Mariottoni. Detection of progressive glaucomatous optic nerve damage on fundus photographs with deep learning. *Ophthalmology*, 2020. [2](#)
- [37] Alexander Miller, Adam Fisch, Jesse Dodge, Amir-Hossein Karimi, Antoine Bordes, and Jason Weston. Key-value memory networks for directly reading documents. In *Proceedings of the 2016 Conference on Empirical Methods in Natural Language Processing*, pages 1400–1409, 2016. [3](#)
- [38] Richard K Parrish, Steven J Gedde, Ingrid U Scott, William J Feuer, Joyce C Schiffman, Carol M Mangione, and Alejandra Montenegro-Piniella. Visual function and quality of life among patients with glaucoma. *Archives of Ophthalmology*, 115(11):1447–1455, 1997. [1](#)
- [39] An Ran Ran, Carol Y Cheung, Xi Wang, Hao Chen, Luyang Luo, Poemen P Chan, Mandy OM Wong, Robert T Chang, Suria S Mannil, Alvin L Young, et al. Detection of glaucomatous optic neuropathy with spectral-domain optical coherence tomography: a retrospective training and validation deep-learning analysis. *The Lancet Digital Health*, 1(4):e172–e182, 2019. [2](#)
- [40] Olaf Ronneberger, Philipp Fischer, and Thomas Brox. U-net: Convolutional networks for biomedical image segmentation. In *International Conference on Medical image computing and computer-assisted intervention*, pages 234–241. Springer, 2015. [11](#), [12](#)
- [41] Pamela A Sample, Christopher A Girkin, Linda M Zangwill, Sonia Jain, Lyne Racette, Lida M Becerra, Robert N Weinreb, Felipe A Medeiros, M Roy Wilson, Julio De León-Ortega, et al. The african descent and glaucoma evaluation study (adages): Design and baseline data. *Archives of ophthalmology*, 127(9):1136–1145, 2009. [6](#), [7](#), [8](#), [12](#), [13](#), [14](#)
- [42] Mark Sandler, Andrew Howard, Menglong Zhu, Andrey Zhmoginov, and Liang-Chieh Chen. Mobilenetv2: Inverted residuals and linear bottlenecks. In *Proceedings of the IEEE conference on computer vision and pattern recognition (CVPR)*, pages 4510–4520, 2018. [2](#), [6](#), [7](#), [8](#), [12](#), [13](#), [14](#)
- [43] Karen Simonyan and Andrew Zisserman. Very deep convolutional networks for large-scale image recognition. In *International Conference on Learning Representations (ICLR)*, 2015. [2](#)
- [44] Jayanthi Sivaswamy, SR Krishnadas, Gopal Datt Joshi, Madhulika Jain, and A Ujjwaft Syed Tabish. Drishti-gs: Retinal image dataset for optic nerve head (onh) segmentation. In *2014 IEEE 11th international symposium on biomedical imaging (ISBI)*, pages 53–56. IEEE, 2014. [14](#)
- [45] Sainbayar Sukhbaatar, Jason Weston, Rob Fergus, et al. End-to-end memory networks. In *Advances in neural information processing systems*, pages 2440–2448, 2015. [5](#)
- [46] Christian Szegedy, Wei Liu, Yangqing Jia, Pierre Sermanet, Scott Reed, Dragomir Anguelov, Dumitru Erhan, Vincent Vanhoucke, and Andrew Rabinovich. Going deeper with convolutions. In *Proceedings of the IEEE conference on computer vision and pattern recognition (CVPR)*, pages 1–9, 2015. [2](#)
- [47] Christian Szegedy, Vincent Vanhoucke, Sergey Ioffe, Jon Shlens, and Zbigniew Wojna. Rethinking the inception architecture for computer vision. In *Proceedings of the IEEE conference on computer vision and pattern recognition*, pages 2818–2826, 2016. [2](#)
- [48] Chuanqi Tan, Fuchun Sun, Tao Kong, Wenchang Zhang, Chao Yang, and Chunfang Liu. A survey on deep transfer

learning. In *International conference on artificial neural networks*, pages 270–279. Springer, 2018. 6

- [49] Mingxing Tan, Bo Chen, Ruoming Pang, Vijay Vasudevan, Mark Sandler, Andrew Howard, and Quoc V Le. Mnasnet: Platform-aware neural architecture search for mobile. In *Proceedings of the IEEE Conference on Computer Vision and Pattern Recognition*, pages 2820–2828, 2019. 2
- [50] Anshul Thakur, Michael Goldbaum, and Siamak Yousefi. Predicting glaucoma before onset using deep learning. *Ophthalmology. Glaucoma*, 3(4):262–268, 2020. 2
- [51] Yih-Chung Tham, Xiang Li, Tien Y Wong, Harry A Quigley, Tin Aung, and Ching-Yu Cheng. Global prevalence of glaucoma and projections of glaucoma burden through 2040: a systematic review and meta-analysis. *Ophthalmology*, 121(11):2081–2090, 2014. 1
- [52] CE Traverso, JG Walt, SP Kelly, AH Hommer, AM Bron, P Denis, JP Nordmann, JP Renard, A Bayer, F Grehn, et al. Direct costs of glaucoma and severity of the disease: a multinational long term study of resource utilisation in europe. *British journal of ophthalmology*, 89(10):1245–1249, 2005. 1
- [53] Isaac Triguero, Salvador García, and Francisco Herrera. Self-labeled techniques for semi-supervised learning: taxonomy, software and empirical study. *Knowledge and Information systems*, 42(2):245–284, 2015. 3, 5
- [54] Jesper E Van Engelen and Holger H Hoos. A survey on semi-supervised learning. *Machine Learning*, 109(2):373–440, 2020. 3
- [55] Yaqing Wang, Quanming Yao, James T Kwok, and Lionel M Ni. Generalizing from a few examples: A survey on few-shot learning. *ACM Computing Surveys (CSUR)*, 53(3):1–34, 2020. 2, 3
- [56] Robert N Weinreb and Peng Tee Khaw. Primary open-angle glaucoma. *The Lancet*, 363(9422):1711–1720, 2004. 1

Supplementary Material

1. Performance Evaluation Metrics

This section provides details on the metrics used in this paper. TP, TN, FP, and FN denote the numbers of true positive, true negative, false positive, and false negative classifications, respectively.

- Accuracy (ACC) refers to the proportion of correct classifications:

$$ACC = \frac{TP + TN}{TP + TN + FP + FN}. \quad (6)$$

It can be a misleading result when the dataset is imbalanced.

- Precision (PRE) measures the proportion of positive classifications that are actually correct:

$$PRE = \frac{TP}{TP + FP}. \quad (7)$$

Network	PRE (%)	REC (%)	ACC (%)	F-score (%)	IoU (%)
U-Net [40]	70.08	67.87	97.93	68.96	52.62
SegNet [1]	79.06	92.68	98.92	85.33	74.41
FCN [30]	88.00	96.79	99.44	92.19	85.51
DeepLabv3+ [7]	96.68	95.93	99.75	96.30	92.87

Table 5: Comparisons of U-Net [40], FCN [30], SegNet [1] and DeepLabv3+ [7] for optic nerve head extraction. The best results are shown in bold type.

- Sensitivity (SEN), also known as recall (REC) or true positive rate (TPR), measures the proportion of positive pixels or images that are correctly classified:

$$SEN = REC = \frac{TP}{TP + FN}. \quad (8)$$

- Specificity (SPE), also known as true negative rate (TNR), measures the proportion of negative pixels or images that are correctly classified:

$$SPE = \frac{TN}{TN + FP}. \quad (9)$$

- F-score is the harmonic mean of PRE and REC:

$$F\text{-score} = 2 \frac{PRE \times REC}{PRE + REC}. \quad (10)$$

It is commonly used in image classification and semantic segmentation tasks, especially when the classes are imbalanced.

- Matthews correlation coefficient (MCC) is a widely used metric to measure the binary classification quality. It is generally regarded as a balanced measurement which can be utilized even if the dataset is imbalanced. Its expression is:

$$MCC = \frac{TP \times TN - FP \times FN}{\sqrt{(TP + FP)(TP + FN)(TN + FP)(TN + FN)}}. \quad (11)$$

- Intersection over union (IoU), also known as Jaccard index, is commonly used in semantic segmentation and object detection to measure the similarity and diversity of sample sets:

$$IoU = \frac{TP}{FN + FP}. \quad (12)$$

- AUC refers to the area underneath the receiver operating characteristic (ROC) curve, whose horizontal and vertical axes are false positive rate (FPR) and TPR, respectively, where $FPR = 1 - TNR$.

Network		OHTS [14]		ACRIMA [11]		LAG [28]		DIGS/ADAGES [41]	
		90% SPE	95% SPE	90% SPE	95% SPE	90% SPE	95% SPE	90% SPE	95% SPE
ResNet-50 [16]	AUC (95% CI)	0.904 (0.865, 0.935)		0.736 (0.698, 0.771)		0.794 (0.780, 0.807)		0.744 (0.696, 0.792)	
	SEN	0.71	0.54	0.38	0.29	0.53	0.42	0.43	0.30
	ACC	0.89	0.93	0.61	0.58	0.77	0.76	0.68	0.64
	FP	1167	584	31	15	314	157	155	78
	FN	175	279	244	280	811	999	792	972
	TP	430	326	152	116	900	712	594	414
	TN	10506	11089	278	294	2829	2986	1395	1472
ResNet-50-LS (ours)	AUC (95% CI)	0.869 (0.833, 0.901)		0.758 (0.723, 0.792)		0.841 (0.829, 0.853)		0.743 (0.683, 0.795)	
	SEN	0.58	0.38	0.45	0.31	0.59	0.45	0.37	0.23
	ACC	0.88	0.92	0.65	0.59	0.79	0.78	0.65	0.61
	FP	1167	584	31	15	314	157	155	78
	FN	253	378	216	272	709	934	868	1073
	TP	352	227	180	124	1002	777	518	313
	TN	10506	11089	278	294	2829	2986	1395	1472
ResNet-50-OVV (ours)	AUC (95% CI)	0.898 (0.857, 0.928)		0.775 (0.741, 0.808)		0.881 (0.870, 0.891)		0.763 (0.695, 0.820)	
	SEN	0.71	0.55	0.37	0.29	0.69	0.57	0.40	0.23
	ACC	0.89	0.93	0.60	0.58	0.83	0.81	0.66	0.61
	FP	1167	584	31	15	314	157	155	78
	FN	177	275	250	281	528	742	835	1062
	TP	428	330	146	115	1183	969	551	324
	TN	10506	11089	278	294	2829	2986	1395	1472

(a) Comparisons of ResNet-50, ResNet-50-LS, and ResNet-50-OVV.

Network		OHTS [14]		ACRIMA [11]		LAG [28]		DIGS/ADAGES [41]	
		90% SPE	95% SPE	90% SPE	95% SPE	90% SPE	95% SPE	90% SPE	95% SPE
MobileNet-v2 [42]	AUC (95% CI)	0.893 (0.845, 0.932)		0.794 (0.760, 0.825)		0.856 (0.844, 0.867)		0.786 (0.728, 0.835)	
	SEN	0.69	0.56	0.52	0.39	0.63	0.53	0.51	0.32
	ACC	0.89	0.93	0.69	0.63	0.80	0.80	0.71	0.65
	FP	1167	584	31	15	314	157	155	78
	FN	186	265	190	243	636	804	686	937
	TP	419	340	206	153	1075	907	700	449
	TN	10506	11089	278	294	2829	2986	1395	1472
MobileNet-v2-LS (ours)	AUC (95% CI)	0.859 (0.813, 0.896)		0.820 (0.786, 0.850)		0.843 (0.831, 0.855)		0.748 (0.689, 0.802)	
	SEN	0.57	0.38	0.54	0.37	0.58	0.43	0.32	0.17
	ACC	0.88	0.92	0.70	0.62	0.79	0.77	0.63	0.58
	FP	1167	584	31	15	314	157	155	78
	FN	258	373	183	249	715	967	942	1156
	TP	347	232	213	147	996	744	444	230
	TN	10506	11089	278	294	2829	2986	1395	1472
MobileNet-v2-OVV (ours)	AUC (95% CI)	0.887 (0.850, 0.920)		0.840 (0.808, 0.867)		0.851 (0.838, 0.862)		0.777 (0.718, 0.826)	
	SEN	0.64	0.46	0.60	0.46	0.63	0.49	0.39	0.19
	ACC	0.89	0.93	0.73	0.68	0.80	0.79	0.66	0.59
	FP	1167	584	31	15	314	157	155	78
	FN	217	328	160	213	641	875	842	1117
	TP	388	277	236	183	1070	836	544	269
	TN	10506	11089	278	294	2829	2986	1395	1472

(b) Comparisons of MobileNet-v2, MobileNet-v2-LS, and MobileNet-v2-OVV.

Table 6: AUC (95% CI), sensitivity, accuracy, FP, FN, TP and TN with respect to 90% specificity and 95% specificity. These results suggest that low-shot learning with multi-task twin neural network and semi-supervised learning with One-Vote Veto self-training perform similarly to supervised learning with respect to different specificities.

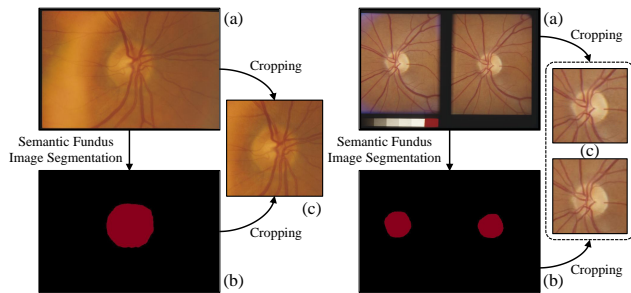
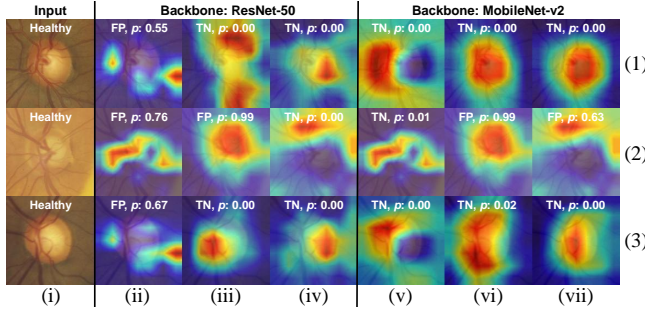


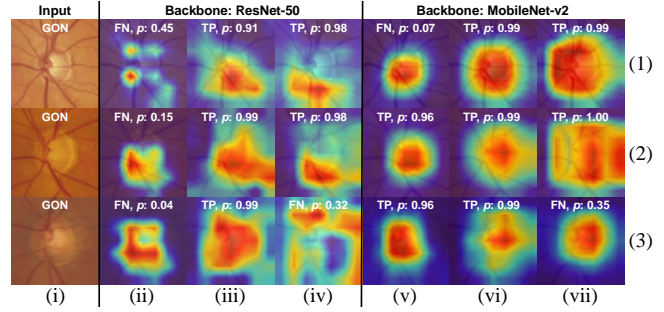
Figure 6: Examples of semantic fundus image segmentation for optic nerve head extraction: (a) raw fundus images; (b) semantic segmentation results, where the optic nerve head areas are shown in red; (c) cropped fundus images used for CNN training.

2. Dataset Preparation

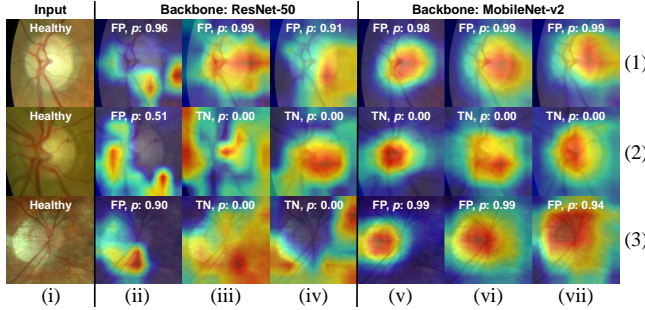
The glaucoma datasets used in our experiments were collected at various intervals by different clinicians from different institutes using different fundus cameras. Since they were gathered for clinical research purposes and not for evaluating computer vision algorithms, this leads to significant variability in image quality and resolution and can make the CNN training much more challenging than expected. To this end, prior to training CNNs for glaucoma diagnosis, we first cropped a region centered on the optic nerve head from each raw fundus image using a semantic segmentation CNN trained for optic nerve head extraction. In our experiments, we trained four semantic segmentation CNNs: 1) U-Net [40], fully convolutional network (FCN) [30], 3) SegNet [1] and 4) DeepLabv3+ [7], on three public optic nerve head segmentation datasets: 1) DRIONS-



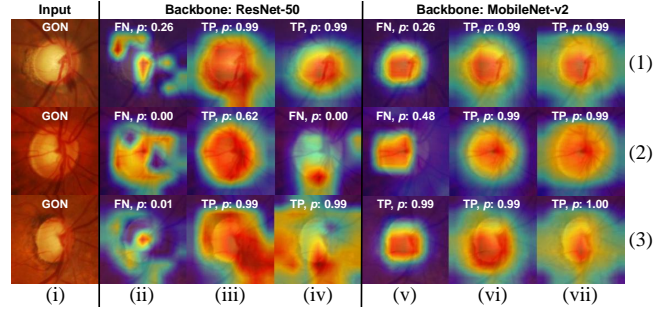
(a) OHTS [14] healthy fundus images.



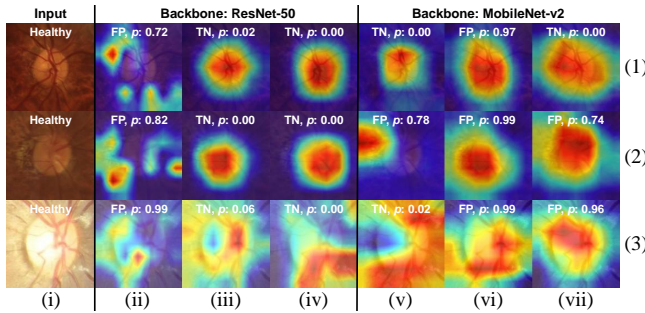
(b) OHTS [14] GON fundus images.



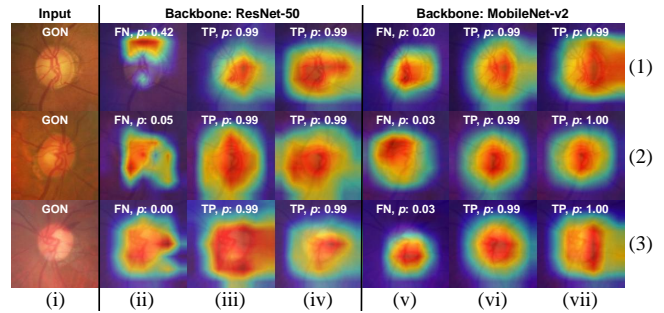
(c) ACRIMA [11] healthy fundus images.



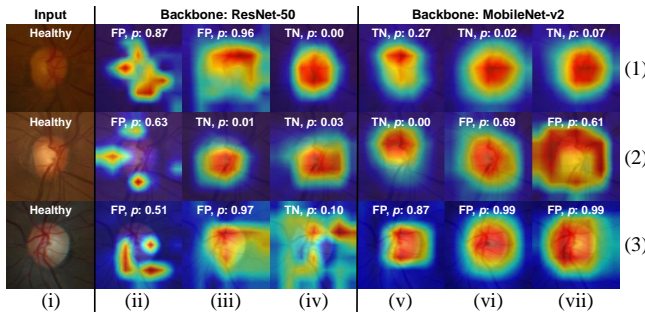
(d) ACRIMA [11] GON fundus images.



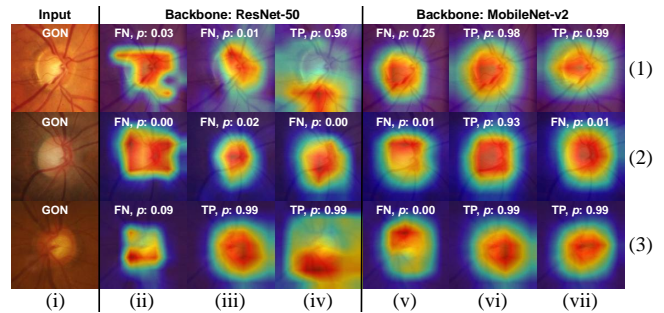
(e) LAG [28] healthy fundus images.



(f) LAG [28] GON fundus images.



(g) DIGS/ADAGES [41] healthy fundus images.



(h) DIGS/ADAGES [41] GON fundus images.

Figure 7: Class activation map visualization examples: (i) fundus images; (ii)-(vii) class activation maps of (i), with respect to ResNet-50 [16], ResNet-LS (ours), ResNet-50-OVV (ours), MobileNet-v2 [42], MobileNet-v2-LS (ours), MobileNet-v2-OVV (ours), respectively. ResNet-50 [16] and MobileNet-v2 [42] are trained with supervised learning using 53K labeled fundus images; ResNet-50-LS and MobileNet-v2-LS are trained with low-shot learning using 1147 labeled fundus images; ResNet-50-OVV and MobileNet-v2-OVV respectively finetune pretrained ResNet-50-LS and MobileNet-v2-LS with semi-supervised learning using 53K fundus images (without ground truth labels). The red regions correspond to high attention, while the blue regions correspond to low attention.

DB [3], 2) Drishti-GS [44], and 3) RIM-ONE [12], which provide the pixel-level optic nerve head ground truth. The quantitative comparisons are shown in Tab. 5, where it can be seen that DeepLabv3+ [7] achieves the best PRE, ACC, F-score and IoU. We then randomly selected 200 fundus images from the OHTS [14] dataset and manually labeled their optic nerve head ground truth to finetune our pretrained DeepLabv3+ [7]. It was subsequently applied to the entire OHTS [14], LAG [28] and DIGS/ADAGES [41] datasets to extract regions centered on the optic nerve heads from raw fundus images. The ACRIMA [11] dataset is already aligned. Examples of the extracted regions are shown in Fig. 6.

3. Supplementary Comparisons of Supervised Learning, Low-Shot Learning and Semi-Supervised Learning

Tab. 1 in the full paper is a subset of Tab. 6 in the supplement. The supplementary comparisons of supervised learning, low-shot learning and semi-supervised learning are shown in Tab. 6. These results suggest that our low-shot learning with multi-task twin neural network and semi-supervised learning with One-Vote Veto (OVV) self-training that require only a small quantity of labeled data, perform similarly and, in some cases, better than the backbone CNNs trained on the entire OHTS [14] training set with supervised learning. Specifically, both ResNet-50-LS and ResNet-50-OVV perform similarly to ResNet-50 [16] on all the four test sets in ACC (varies by less than 3%) with respect to both 90% specificity and 95% specificity. MobileNet-v2-LS and MobileNet-v2-OVV perform similarly on the OHTS [14] and LAG [28] test sets in ACC with respect to both 90% specificity and 95% specificity. Although their achieved ACC is lower (decreases by 5 – 8%) than that of MobileNet-v2 [42] on the DIGS/ADAGES [41] test set, the ACC increases by up to 4% on the ACRIMA [11] dataset.

4. Class Activation Map Visualization

We next utilize Grad-CAM++ [6] to explain the models compared in Tab. 6, as shown in Fig. 7. These results suggest that the optic nerve head areas have the greatest impact on model decisions. The neuroretinal rim areas are identified as most important and the periphery contributed comparatively little to model decisions for both healthy and glaucomatous optic neuropathy (GON) eyes [8].